Research Article | Vol. 34, No. 17 / 24 Aug 2026 / *Optics Express* 32584

Optics EXPRESS

Heterogeneously integrated E-band InP-on-Si tunable laser via micro-transfer printing

DONGBO WANG,[1,2,*] EMADREZA SOLTANIAN,[1,2] SENBIAO QIN,[1,2] NICOLAS VAISSIERE,[3] DELPHINE NÉEL,[3] JOAN RAMIREZ,[3] JEAN DECOBERT,[3] BART KUYKEN,[1,2] JING ZHANG,[1,2] AND GUNTHER ROELKENS[1,2]

[1] *Photonics Research Group, Ghent University - imec, 9052 Ghent, Belgium*
[2] *Center for Nano- and Biophotonics, Ghent University, Ghent, Belgium*
[3] *III-V Lab, a joint laboratory between Nokia Bell Labs, Thales Research & Technology and CEA-LETI, F91767 Palaiseau, France*
[*] *Dongbo.Wang@UGent.be*

Abstract: We demonstrate a widely tunable E-band InP-on-Si laser heterogeneously integrated using micro-transfer printing (μTP). The InP-based quantum-well gain material is designed with a photoluminescence peak centered around 1400 nm. Pre-fabricated InP semiconductor optical amplifiers (SOAs) are micro-transfer printed onto the IMEC 200 mm silicon-on-insulator (SOI) photonics platform. Using a silicon Vernier filter, continuous wavelength tuning from 1398 to 1439 nm is achieved, corresponding to a 41 nm tuning range spanning the upper E-band. The laser exhibits a side-mode suppression ratio exceeding 45 dB over the entire tuning range and delivers up to 3 mW output power in the silicon waveguide. A relative intensity noise (RIN) level down to −145 dBc/Hz is measured, indicating low-noise operation relevant for optical communication applications.

1. Introduction

Silicon photonics provides a mature platform for photonic integrated circuits (PICs), leveraging CMOS-compatible processing, large-wafer manufacturing infrastructure, and a rich library of components [1]. However, silicon lacks efficient optical gain because of its indirect bandgap, making the integration of III–V gain materials a key route toward lasers and semiconductor optical amplifiers (SOAs) on silicon photonics platforms [2]. Over the past decade, different III–V/Si integration approaches have been developed, including direct epitaxial growth, flip-chip integration, wafer bonding, and micro-transfer printing (μTP) [3–6]. These approaches combine III–V materials with silicon photonic circuits and have enabled a broad range of integrated laser sources. In parallel, single-mode lasers based on wavelength-selective feedback, including distributed gratings, sampled-grating distributed Bragg reflector (SG-DBR) sections, and Vernier ring-resonator filters, have been extensively investigated for O-band and C-band wavelength-division multiplexing and coherent optical communication systems [7–11].

The E-band (1360–1460 nm), historically limited by the OH-related absorption peak near 1383 nm, has become more accessible with the development of low-water-peak fibers. A recent demonstration of 30-Gbaud PM-16-QAM transmission over 50 km of G.652.D fiber in the 1405–1430 nm range confirms the communication potential of the upper E-band [12]. This wavelength range also overlaps with water-related tunable-diode-laser spectroscopy around 1400 nm [13], providing an additional motivation for compact wavelength-agile sources. However, most silicon-based tunable lasers have so far targeted the O-band, C-band, L-band, or longer wavelengths [14,15], leaving E-band integrated tunable lasers comparatively underdeveloped.

#607214
Journal © 2026

https://doi.org/10.1364/OE.607214
Received 1 Jun 2026; revised 7 Aug 2026; accepted 7 Aug 2026; published 19 Aug 2026

Recently, a wafer-bonded E-band tunable laser covering 1350–1408 nm has been reported, demonstrating the feasibility of heterogeneous E-band laser operation on silicon [16]. That demonstration mainly addresses the lower E-band, while the upper E-band remains less explored. Extending operation to this range requires III–V gain material with a shifted spectrum. Furthermore, wafer bonding typically integrates III–V material over relatively large areas, whereas μTP enables localized placement of pre-fabricated III–V gain coupons on processed silicon photonic wafers. This allows the III–V gain devices and silicon photonic circuits to be fabricated, optimized, and tested separately before integration, offering a flexible route for scalable E-band laser integration. The localized and decoupled process is attractive for cost-effective multi-wavelength integration, since the III–V gain material can be redesigned for the target band while the silicon photonic platform and the general μTP integration flow can largely be reused.

In this work, we demonstrate an E-band InP-on-Si tunable laser heterogeneously integrated on IMEC's 200 mm silicon photonics pilot line using micro-transfer printing. The laser employs an extended-cavity architecture consisting of a transfer-printed InP SOA, a silicon Vernier filter formed by two thermally tunable micro-ring resonators, a thermo-optic phase tuning section, and a tunable loop mirror for output coupling. The InP-based quantum well gain is designed for E-band operation, with a photoluminescence peak around 1400 nm. The silicon PIC is fabricated in IMEC's silicon photonics line using a 220 nm thick silicon device layer and a full back-end stack. Continuous wavelength tuning from 1398 to 1439 nm is achieved, corresponding to a 41 nm tuning range across the upper E-band. The laser exhibits a side-mode suppression ratio exceeding 45 dB over the entire tuning range and delivers up to 3 mW output power in the silicon waveguide. A relative intensity noise down to −145 dBc/Hz is measured, indicating low-noise operation of the integrated laser. This work provides a scalable route toward micro-transfer-printed E-band tunable lasers on silicon photonics platforms.

2. Cavity design and III–V epitaxy

The tunable laser is based on an extended-cavity architecture combining passive silicon photonic circuits with a transfer-printed InP SOA. A schematic layout of the laser cavity is shown in Fig. 1. The SOA has a length of 1.2 mm and includes one adiabatic taper on each side to couple light between the III–V waveguide and the underlying silicon waveguide. The adiabatic taper is 180 μm long, with the III–V mesa width reduced from 3 μm to 0.6 μm. This taper design relaxes the lateral alignment requirement for μTP and provides tolerance compatible with the ±1.5 μm (3σ) alignment accuracy of lab-scale micro-transfer-printing tools [17].

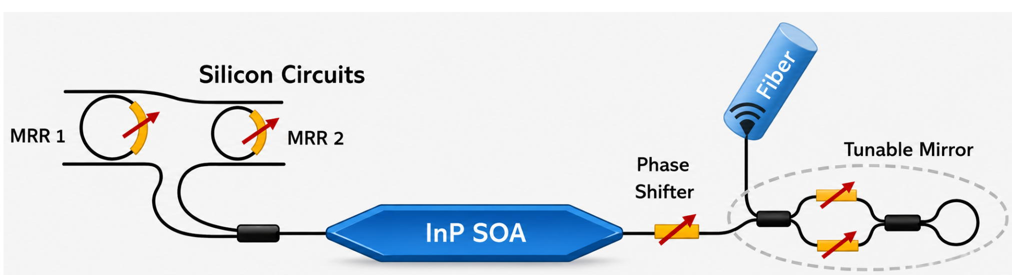

Fig. 1. Schematic layout of the InP-on-Si tunable laser cavity.

Wavelength selection is achieved by two thermally tunable silicon micro-ring resonators (MRRs) with slightly different radii of 24 μm and 22 μm. The individual ring resonators have an free spectral range (FSR) of approximately 3.9 nm in the targeted wavelength range. Together, the two MRRs form a Vernier filter with an effective FSR of approximately 25 nm, resulting in a

Optics EXPRESS

wider tuning range. A thermo-optic phase tuning section is included to align the longitudinal cavity modes with the selected Vernier resonance. The other side of the cavity is formed by a Mach–Zehnder interferometer (MZI)-based tunable Sagnac loop mirror, which serves as a reflectivity-adjustable output coupler. By tuning the phase difference between the two MZI arms, the effective reflectivity and output-coupling strength of the mirror can be adjusted.

The III–V epitaxial layer stack was grown on a 2-inch InP substrate by metal-organic vapor-phase epitaxy (MOVPE). To shift the gain spectrum towards the E-band, the active region was designed with six Al-containing quantum wells, resulting in a photoluminescence (PL) peak centered around 1400 nm. The Al-containing quantum-well design maintains higher quantum efficiency under high-temperature operation. Separate-confinement heterostructure (SCH) layers are incorporated around the active region to improve optical confinement and facilitate electrical injection into the quantum wells. An AlInAs sacrificial layer is included beneath the device stack to enable selective under-etching and coupon release from the native InP substrate for the μTP process.

3. Device fabrication

The fabrication flow consists of two main parts, as illustrated in Fig. 2: the preparation of the InP-based III–V SOA coupons on the source wafer and the silicon photonics process on the target wafer, followed by micro-transfer printing and post-printing metallization.

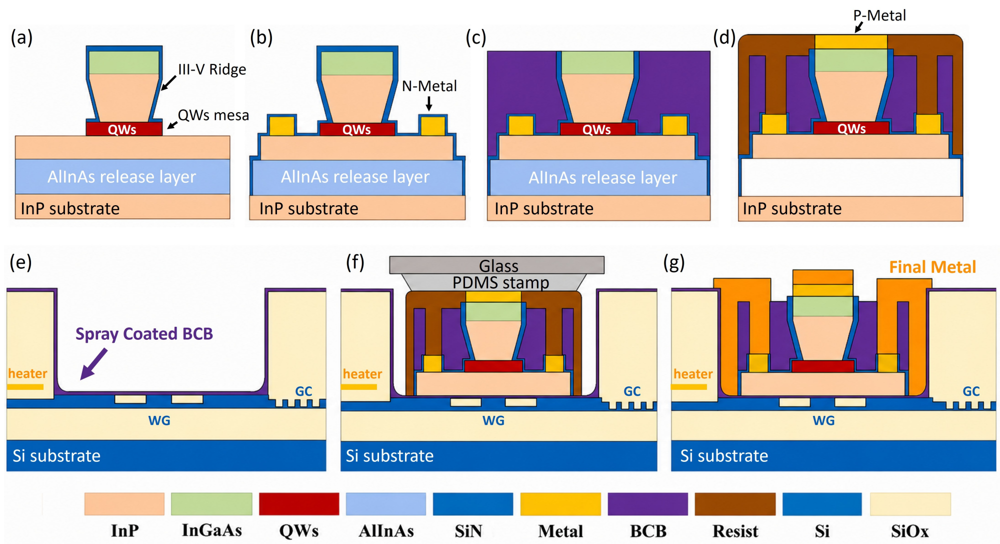

Fig. 2. Schematic process flow for the micro-transfer-printed InP-on-Si tunable laser: (a) InP SOA mesa definition, (b) n-metal and tether formation, (c) BCB planarization and etch-back, (d) release etching, (e) target wafer preparation, (f) micro-transfer printing into the predefined recess, (g) final metallization.

The SOA coupons were fabricated on the InP source wafer by III–V Lab using a sequence of electron-beam and optical lithography steps, combined with wet and dry etching processes and metal contact deposition. First, the III–V ridge and quantum-well mesa were patterned using a SiN hard mask, as shown in Fig. 2(a). The n-contact metal was then deposited, followed by etching of the n-InP layer, the lattice-matched InGaAs (50 nm) and AlInAs (500 nm) release layers, and several hundred nanometers into the InP substrate. An approximately 500 nm thick SiN layer was subsequently deposited and patterned to form tethers, which hold the coupons in place during the selective release etch, as shown in Fig. 2(b). The devices were then planarized with a thick benzocyclobutene (BCB) layer, followed by a blanket etch-back until the top p-InGaAs contact layer was exposed, as shown in Fig. 2(c). To reinforce the tethers during the critical coupon release step, a Ti35E photoresist layer was spin-coated and patterned as auxiliary support structures following the SiN-tether geometry. After wet etching in $FeCl_3$ for 1 h, the release layer was selectively removed and the coupons became suspended, while remaining attached to the source wafer by the tethers. $FeCl_3$ was selected as an optimized release etchant to minimize coupon backside dishing caused by the finite selectivity of the etching solution [18]. At this stage, the coupons were ready for micro-transfer printing, as shown in Fig. 2(d).

The silicon PIC was fabricated in IMEC's 200 mm silicon photonics pilot line on the Passives+ platform, comprising a 220 nm Si device layer, a 160 nm poly-Si layer, tungsten heaters, metal routing, and local openings for III–V integration. The opened recess on the target chip was designed to be slightly larger than the pre-fabricated III–V SOA coupon. Prior to printing, a BCB adhesive layer was spray-coated on the target wafer, as shown in Fig. 2(e). This layer promotes adhesion between the III–V coupon and the silicon photonics chip during printing, resulting in an approximately 30–40 nm bonding layer after printing and full curing. The coating step was followed by a soft bake at 80 °C for 2 min and a gradual temperature ramp to 150 °C for 15 min.

Micro-transfer printing of the III–V SOAs was performed using an X-Celeprint μTP-100 lab-scale printer. The process uses an elastomeric polydimethylsiloxane (PDMS) stamp to pick up and print the released SOA coupons. A dedicated stamp with dimensions matched to the coupon size was used to pick up the coupon from the source wafer by breaking the tethers, and then to laminate it onto the adhesive-coated recess on the target silicon photonics wafer, as shown in Fig. 2(f). After lamination, the stamp was slowly peeled off and reused for the next printing cycle. After printing, a 90 min oxygen plasma etch was performed to remove the photoresist encapsulation from the printed III–V SOAs. The post-printing process was completed by electrically connecting the printed SOAs to the silicon photonics back-end pads using a 1 μm thick Au metallization layer patterned by lift-off, as shown in Fig. 2(g). To ensure continuous metal coverage across the 6.5 μm-deep recess and the printed-coupon topography, the Au metallization was deposited by electron-beam evaporation with the sample mounted on a 30° tilted stage under continuous rotation.

Figure 3(a) shows a microscope image of the standalone single-ring resonator with integrated heaters, used for passive resonator characterization. Figure 3(b) shows released InP coupons on the source wafer after sacrificial-layer removal, together with several empty coupon sites after pick-up. The coupons remain suspended and anchored by the SiN tethers before pick-up. After coupon detachment, the SiN tethers remain on the source wafer. Figure 3(c) shows a microscope image of the fabricated silicon Vernier filter. Figure 3(d) shows a transfer-printed InP coupon placed inside the predefined recess on the target silicon photonics chip, corresponding to the printing step shown in Fig. 2(f). The tether-like traces visible near the printed coupon originate from the auxiliary photoresist support structures rather than from residual SiN tethers. Figure 3(e) shows a zoomed-in view of the alignment. The lateral misalignment between the printed III–V coupon and the underlying silicon waveguide is below 500 nm. Figure 3(f) shows the finished InP-on-Si tunable laser after final metallization.

Optics EXPRESS

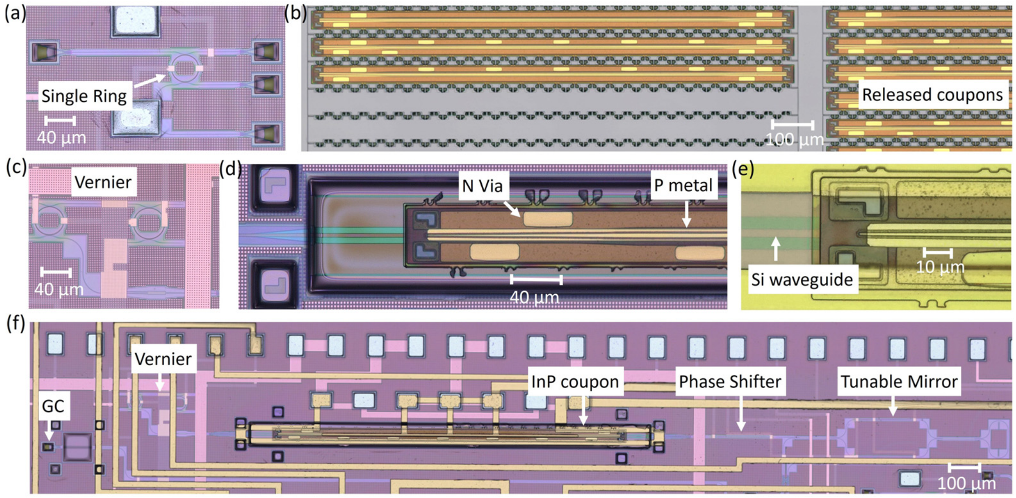

Fig. 3. (a) Microscope image of the standalone single-ring resonator with heaters. (b) Released InP coupons and empty sites on the source wafer. (c) Fabricated silicon Vernier filter. (d) Transfer-printed InP coupon in the predefined recess. (e) Zoomed-in view of the alignment. (f) Finished InP-on-Si tunable laser after final metallization.

4. Characterization

4.1. Passive ring resonator characterization

The performance of a Vernier-filter-based tunable laser is strongly influenced by the passive ring resonators, since their resonance linewidth, insertion loss, and thermal tuning efficiency determine the wavelength selectivity and round-trip loss of the external cavity. For a given platform, the loaded quality factor and resonance extinction are mainly governed by the coupling strength between the ring and the bus waveguide, which is controlled by the coupling gap [19]. In this work, the ring resonators are designed using a 610 nm wide rib waveguide and a 350 nm coupling gap. The propagation loss of the silicon waveguide is approximately 1 dB/cm. A standalone add-drop MRR with the same heater design, shown in Fig. 3(a), is included on the chip to measure the passive ring response and thermal tuning behavior.

Figure 4(a) shows the measured through-port transmission spectra of the standalone MRR under different heater powers. The resonance shifts with increasing heater power, while the resonance shape remains stable over the tuning range. The extracted phase shift as a function of heater power is shown in Fig. 4(b). A heater power of approximately 78 mW is required to induce a 2π round-trip phase shift, corresponding to a resonance shift of one free spectral range (~3.9 nm). The extracted loaded quality factor remains between 8500 and 9800 during thermal tuning, indicating that the heater operation does not significantly change the coupling condition. This confirms that the ring resonators provide stable wavelength-selective feedback for Vernier tuning in the laser cavity.

4.2. Laser characterization

The heterogeneously integrated tunable laser was characterized on a temperature-controlled stage at 18 °C using a thermo-electric cooler (TEC). Electrical contacts to the InP SOA and the thermal tuning elements were made using direct-current (DC) probes. Multiple Keithley 2400 source meters were used to bias the gain section, the two MRR heaters, the phase tuning section, and the tunable loop mirror. The laser output was collected from the silicon grating coupler using a

Optics EXPRESS

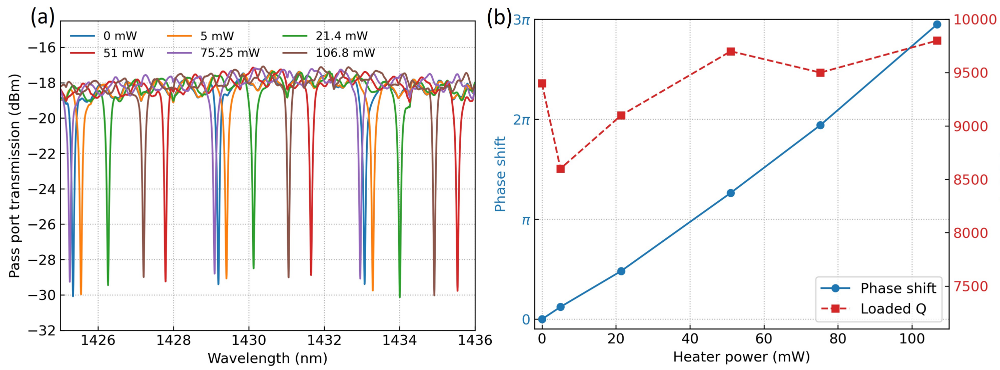

Fig. 4. (a) Through-port transmission spectra of the standalone MRR under heater tuning. (b) Extracted phase shift and loaded quality factor as a function of heater power

cleaved standard single-mode fiber. A reference silicon waveguide with identical grating couplers on both sides was included on the same chip to calibrate the grating-coupler loss.

Figure 5(a) shows the measured transmission spectrum of the reference waveguide. The extracted coupling loss is approximately 8–10 dB per grating coupler over the 1400–1450 nm wavelength range. The laser output was then characterized using an optical power meter (HP 8153A) and an optical spectrum analyzer (Anritsu MS9740A). Figure 5(b) shows a typical light-current-voltage (LIV) curve of the laser, measured by sweeping only the gain current while keeping all heater biases fixed. The laser has a threshold current of approximately 70 mA and a differential resistance of 18 Ω extracted from the I–V curve. After correcting for the grating-coupler loss, the output power in the silicon waveguide reaches 3 mW at a gain current of 124 mA. The periodic oscillation of the output power originates from the thermally induced phase changes in the gain section, which shift the cavity mode positions. Higher output power appears when the cavity mode aligns with the MRR resonance, whereas reduced output power occurs when the cavity mode is detuned from the resonance.

The optical spectra at different operating wavelengths are shown in Fig. 5(c). The spectra were measured with an optical spectrum analyzer using a resolution of 30 pm. By tuning the two MRR heaters together with the phase section and tunable loop mirror, single-mode lasing is obtained from 1398 to 1439 nm, corresponding to a 41 nm tuning range. The side-mode suppression ratio remains above 45 dB over the entire tuning range. As expected, the wavelength tuning exceeds a single Vernier FSR [20].

In single-mode semiconductor lasers, carrier recombination and photon generation lead to instantaneous fluctuations in the intracavity photon density. These fluctuations appear as variations in the output optical power, described as the relative intensity noise (RIN) [21]. A low RIN is important for optical transmitters, since excess intensity noise directly degrades the signal-to-noise ratio of intensity- or coherently modulated optical links. To evaluate the RIN of the InP-on-Si laser in this work, the emitted light was coupled into a high-speed photodetector with a transimpedance amplifier (Discovery DSCR409). The converted electrical signal was passed through a DC block to remove the DC component and then amplified by a radio-frequency (RF) amplifier (SHF S804B). The resulting RF signal was recorded using an electrical spectrum analyzer (Keysight N9010A). The measured RF noise contains contributions from the laser intensity noise, photodetector shot noise, and the thermal/electronic noise of the RF amplifier and transimpedance amplifier. To extract the laser RIN, the system noise floor was measured with the laser switched off and subtracted from the RF spectra before normalization to the detected photocurrent and resolution bandwidth.

Optics EXPRESS

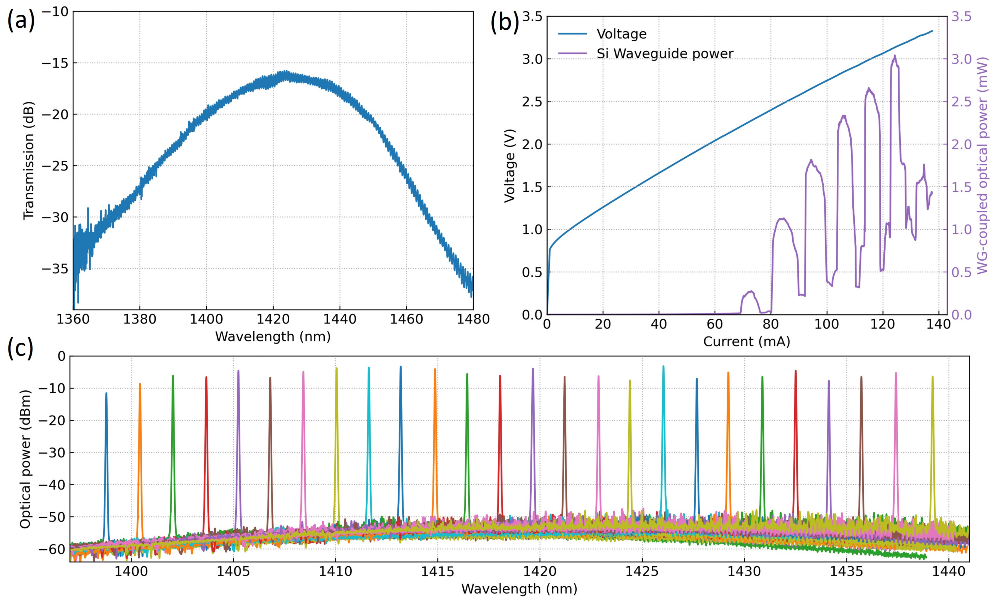

Fig. 5. (a) Transmission spectrum of the reference waveguide with grating couplers on both sides. (b) Light-current-voltage curve of the InP-on-Si tunable laser. (c) Optical spectra at different operation wavelengths.

Figure 6(a) shows the optical spectra of the laser at different SOA injection currents. During this measurement, the gain current was swept, while the ring-filter heater biases were slightly adjusted to maximize the output power at each current setting. The lasing peak slightly redshifts with increasing current due to the thermal effect, while stable single-mode operation with high SMSR above 50 dB is maintained.

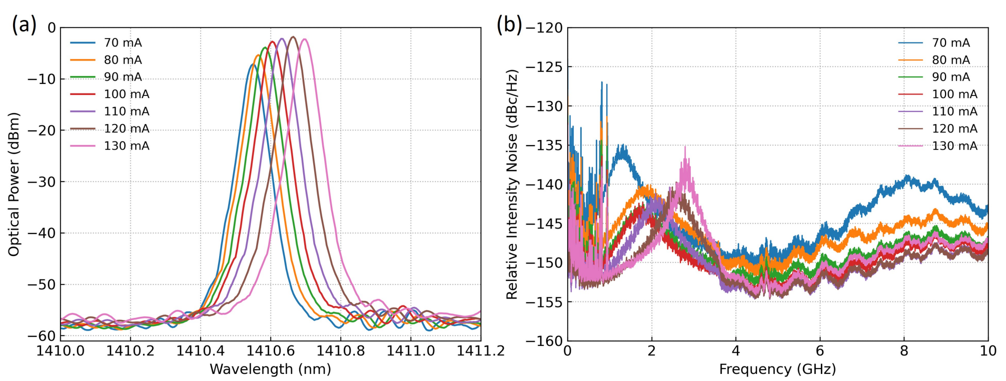

Fig. 6. (a) Optical spectra at different SOA injection currents. (b) RIN spectra at different SOA injection currents.

The RIN spectra at different SOA currents are shown in Fig. 6(b). A prominent relaxation oscillation peak is observed and shifts towards higher frequencies as the injection current increases. This behavior is consistent with the increase of relaxation oscillation frequency with carrier-photon coupling strength and intracavity photon density, which typically follows a square-root dependence on the current above threshold [22]. At the same time, the overall

Research Article | Vol. 34, No. 17 / 24 Aug 2026 / Optics Express 32591
Optics EXPRESS

RIN level decreases as the laser is biased further above threshold. This reduction is mainly attributed to the increased photon number in the cavity, which reduces the relative contribution of spontaneous-emission-induced photon number fluctuations. At higher bias currents, the RIN reaches values below −145 dBc/Hz over a broad frequency range, indicating low-noise operation of the integrated E-band laser.

4.3. Laser tuning and control

A two-dimensional sweep of the MRR heaters was performed to characterize the tuning map for the laser. Figure 7(a) shows the lasing wavelength as a function of the two ring heater powers. During this measurement, the two ring heaters were swept in a nested manner, while the gain current was fixed at 100 mA and the phase tuning section and tunable loop reflector were kept at constant bias. At each heater setting, the optical spectrum was recorded, and the dominant lasing wavelength was extracted. The periodic pattern in the map reflects the Vernier selection mechanism between the two ring resonators. The tuning map can be used as a lookup table to rapidly access a target wavelength. Figure 7(b) shows the lasing wavelength during single-ring heater tuning. The effective lasing-wavelength tuning slopes are extracted to be approximately 0.44 nm/mW and −0.61 nm/mW, respectively.

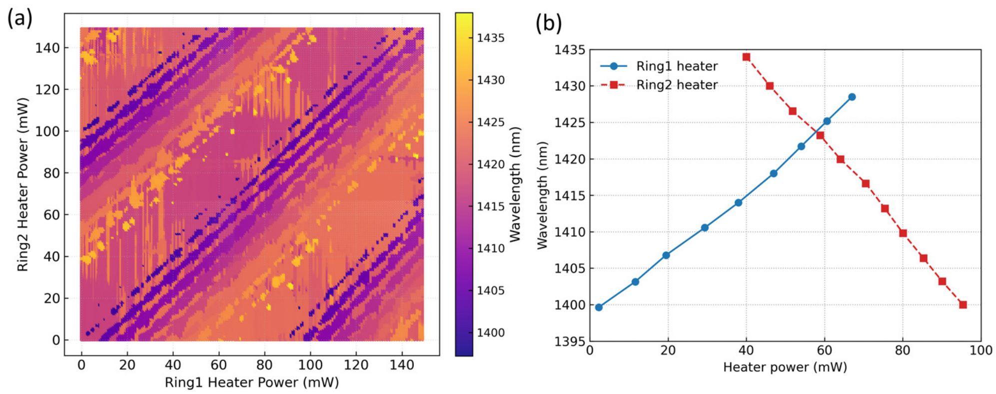

Fig. 7. (a) 2D lasing-wavelength map as a function of the two ring heater powers. (b) Lasing wavelength during single-ring heater tuning.

A tunable Sagnac loop mirror is implemented as the out-coupling mirror of the laser cavity. By tuning the phase difference between the two MZI arms, the effective reflectivity of the loop mirror and hence the output-coupling strength can be controlled. This allows the trade-off between optical feedback to the cavity and power extraction from the cavity to be adjusted. Figure 8(a) shows the light-current (LI) curves measured at different heater powers on one MZI arm. For each heater bias, the threshold current is extracted from the LI curve and plotted in Fig. 8(b). The highest threshold current is observed at a heater bias of 26.34 mW, where the loop mirror provides lower effective reflectivity and stronger output coupling, resulting in increased mirror loss for the laser cavity.

Figure 8(b) also shows the fiber-coupled output power measured by sweeping the heater on one MZI arm, while keeping the SOA current fixed at 110 mA and the MRR heaters and phase tuning section at fixed bias points. The output power exhibits a periodic dependence on the heater power. It is strongly suppressed around 5 mW and 47 mW, corresponding to mirror settings with weak output coupling. The 42 mW separation between these two suppressed-output points corresponds to a 2π phase shift of the MZI arm heater. The maximum fiber-coupled output power is obtained around 25 mW, where the mirror bias provides stronger output coupling, consistent with the increased threshold current.

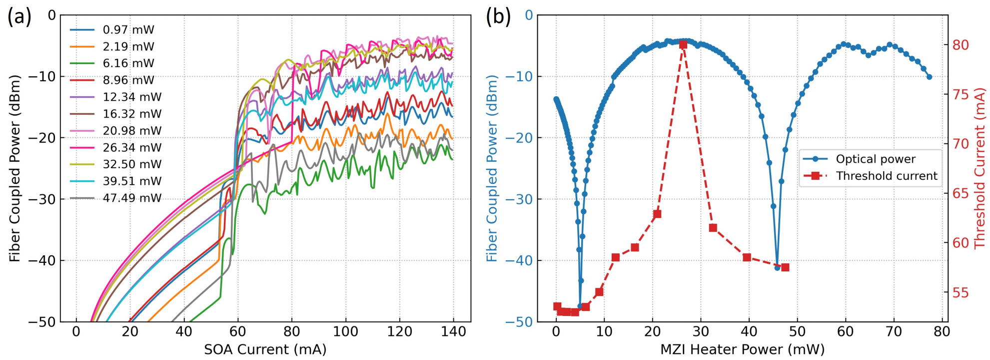

Fig. 8. (a) LI curves measured at different heater powers on one MZI arm. (b) Fiber-coupled output power and extracted threshold current as a function of the heater power on one MZI arm.

5. Conclusion

We demonstrated a heterogeneously integrated E-band InP-on-Si tunable laser on the IMEC 200 mm silicon photonics platform using micro-transfer printing. The laser combines a transfer-printed InP SOA with a silicon Vernier filter, a thermo-optic phase tuning section, and an MZI-based tunable Sagnac loop mirror. The InP quantum-well gain material was designed for E-band operation, with a photoluminescence peak around 1400 nm. Continuous wavelength tuning from 1398 to 1439 nm was achieved, corresponding to a 41 nm tuning range across the upper E-band. The laser maintained single-mode operation with a SMSR above 45 dB, delivered up to 3 mW output power in the silicon waveguide, and showed a RIN level down to −145 dBc/Hz. These results demonstrate the potential of micro-transfer printing for integration of wavelength-specific III–V gain materials on silicon photonics platforms, providing a scalable route toward E-band tunable laser sources.

Funding. European Union (871345, 101139777).

Disclosures. The authors declare no conflicts of interest.

Data availability. Data underlying the results presented in this paper are not publicly available at this time but may be obtained from the authors upon reasonable request.

References

1. S. Shekhar, W. Bogaerts, L. Chrostowski, *et al.*, “Roadmapping the next generation of silicon photonics,” Nat. Commun. **15**(1), 751 (2024).
2. D. Liang and J. E. Bowers, “Recent progress in heterogeneous III-V-on-silicon photonic integration,” Light: Advanced Manufacturing **2**(1), 59–83 (2021).
3. S. Chen, W. Li, J. Wu, *et al.*, “Electrically pumped continuous-wave III–V quantum dot lasers on silicon,” Nat. Photonics **10**(5), 307–311 (2016).
4. A. Marinins, S. Hänsch, H. Sar, *et al.*, “Wafer-scale hybrid integration of InP DFB lasers on Si photonics by flip-chip bonding with sub-300 nm alignment precision,” IEEE J. Sel. Top. Quantum Electron. **29**(6: Photonic Signal Processing), 1–9 (2023).
5. A. W. Fang, H. Park, O. Cohen, *et al.*, “Electrically pumped hybrid AlGaInAs–silicon evanescent laser,” Opt. Express **14**(20), 9203–9210 (2006).
6. G. Roelkens, J. Zhang, L. Bogaert, *et al.*, “Present and future of micro-transfer printing for heterogeneous photonic integrated circuits,” APL Photonics **9**(1), 010901 (2024).
7. J. R. Vaskasi, N. Singh, J. V. Kerrebrouck, *et al.*, “High wall-plug efficiency and narrow linewidth III-V-on-silicon C-band DFB laser diodes,” Opt. Express **30**(15), 27983–27992 (2022).
8. H. Duprez, C. Jany, C. Seassal, *et al.*, “Highly tunable heterogeneously integrated III-V on silicon sampled-grating distributed Bragg reflector lasers operating in the O-band,” Opt. Express **24**(18), 20895–20903 (2016).
9. S. Lin, X. Zheng, J. Yao, *et al.*, “Efficient, tunable flip-chip-integrated III-V/Si hybrid external-cavity laser array,” Opt. Express **24**(19), 21454–21462 (2016).

10. P. A. Morton, C. Xiang, J. B. Khurgin, *et al.*, "Integrated coherent tunable laser (ICTL) with ultra-wideband wavelength tuning and sub-100 Hz Lorentzian linewidth," J. Lightwave Technol. **40**(6), 1802–1809 (2022).
11. C. Yang, L. Liang, L. Qin, *et al.*, "Advances in silicon-based, integrated tunable semiconductor lasers," Nanophotonics **12**(2), 197–217 (2023).
12. A. Donodin, L. Kiani, S. Noor, *et al.*, "E-band transmission of 30-Gbaud PM-16-QAM supported by neodymium-doped fiber amplifier," in *Optical Fiber Communication Conference (OFC) 2024*, (Optica Publishing Group, 2024), p. W1D.4.
13. K. Duan, L. Ma, Y. Yi, *et al.*, "Tunable diode laser-based two-line thermometry: a noncontact thermometer for active body temperature measurement," Appl. Opt. **60**(23), 7036–7042 (2021).
14. E. Soltanian, G. Muliuk, S. Uvin, *et al.*, "Micro-transfer-printed narrow-linewidth III-V-on-Si double laser structure with a combined 110 nm tuning range," Opt. Express **30**(22), 39329–39339 (2022).
15. X. Guo, E. Soltanian, J. Zhang, *et al.*, "Micro-transfer-printed short-wave infrared InP-on-silicon tunable laser," Opt. Lett. **50**(5), 1589–1592 (2025).
16. J. Guo, C. Xiang, T. J. Morin, *et al.*, "E-band widely tunable, narrow linewidth heterogeneous laser on silicon," APL Photonics **8**(4), 046114 (2023).
17. B. Haq, S. Kumari, K. Van Gasse, *et al.*, "Micro-transfer-printed III-V-on-silicon C-band semiconductor optical amplifiers," Laser & Photonics Reviews **14**(7), 1900364 (2020).
18. A. D. Groote, P. Cardile, A. Z. Subramanian, *et al.*, "Transfer-printing-based integration of single-mode waveguide-coupled III-V-on-silicon broadband light emitters," Opt. Express **24**(13), 13754–13762 (2016).
19. W. Bogaerts, P. De Heyn, T. Van Vaerenbergh, *et al.*, "Silicon microring resonators," Laser & Photonics Reviews **6**(1), 47–73 (2012).
20. B. Pan, J. Bourderionnet, V. Billault, *et al.*, "III-V-on-Si3N4 widely tunable narrow-linewidth laser based on micro-transfer printing," Photonics Res. **12**(11), 2508–2520 (2024).
21. L. A. Coldren, S. W. Corzine, and M. L. Mashanovitch, *Diode lasers and photonic integrated circuits* (John Wiley & Sons, 2012).
22. G. Morthier and P. Vankwikelberge, *Handbook of distributed feedback laser diodes* (Artech House, 2013).